

Fig. 1. Hollow *Listeria* cytoplasmic comet tail contains closely packed parallel filaments. (A) Slice through the tomogram of a cytoplasmic comet tail (tail) in a PtK2 cell (cytoplasm is indicated by cyt) infected by *Listeria* (b). (Scale bar: 200 nm.) Distribution of XY-filaments (B) and Z-filaments (C) in the XZ plane, projected over the Y axis. The color scale ranges from high occurrence (red) to low occurrence (blue) (same color code in all relevant panels). (D) Two-dimensional histogram of interfilament distances, weighted by the distance, and relative orientations between the filaments. deg, degrees. (E) Two-dimensional histogram of the (ξ , ζ) coordinates of the neighboring filaments in an XY-bundle in the local plane perpendicular to the central filament (dark gray, drawn to scale). (F) XY-filaments projected into the XY plane. The color of the filaments corresponds to their angle with respect to the Y axis: 0–15° (blue), 15–30° (green), 30–45° (red). The cell wall of the bacterium is shown in gray. (G) XY-pairs of parallel filaments (black) among XY-filaments (orange).

experiments were performed on thin areas of the cell. In the data presented, the bacterium moves within the confines of the thin cytoplasm in the plane of the substrate; therefore, the comet tails described are not rotationally symmetrical about the long axis of the network (Fig. S7). Instead of using the long axis of the comet tail as the frame of reference, we used the substrate plane. This also permits the analysis of the other cellular networks explored here.

The XY plane of the substrate was defined using principal component analysis of the coordinates of the filaments (SI Text). In our Cartesian coordinate system, the Y axis is defined along the long axis of the network, which usually coincides with the long axis of the bacterium in the case of comet tails. The X axis is associated with the width of the network on the plane of the substrate. The Z axis is perpendicular to the XY plane and corresponds to the thickness of the network. We distinguish between filaments with a deviation out of the XY plane toward Z smaller than 30° (“XY-filaments”) and filaments with a deviation larger than 30° (“Z-filaments”). We defined 30° as the inclination limit, above which filaments do not belong to the XY plane.

Filaments Tangential to the Bacterial Surface Contribute to the Comet Tail Architecture During Intracellular Movement and Cell-to-Cell Spread. The majority of the filaments are XY-filaments both in cytoplasmic comet tails (73%) and in protrusions (89%), and they are typically 200–300 nm in length (Table S1). In cytoplasmic comet tails, XY-filaments exist in high density (Figs. S1B and S2B), enveloping the pole of the bacteria tangentially (Fig. 1F and Figs. S1E and S2F). One of five cytoplasmic comet tails was found to be almost depleted of internal XY-filaments (Fig. 1B). A similar, nearly hollow shell structure of XY-filaments is observed in protrusions, where they are mainly found in the vicinity of the membrane (Fig. 2B and Fig. S4B; five of nine

tomograms). In cytoplasmic comet tails and in protrusions, Z-filaments are typically 150 nm long; they appear throughout the entire tail, coating the bacterial pole tangentially (Figs. 1C and 2C and Figs. S1C, S2C, and S4 C and F). Interestingly, XY- and Z-filaments are tangential to the bacterial surface.

Cytoplasmic Comet Tails and Protrusions Contain Closely Packed Parallel Filaments. To analyze quantitatively comet tail architecture, we determined distances and relative orientations (angles) between filaments (SI Text and Figs. S8 and S9). For interfilament angles between 0° and 15° (i.e., a nearly parallel orientation), we found spacings of 12.8 ± 1.1 nm in cytoplasmic comet tails (Fig. 1D and Figs. S1D and S2D) and spacings of 12.3 ± 0.8 nm in protrusions (Fig. 2D and Fig. S4 K and M). Several bundling/cross-linking proteins have been localized in *Listeria* comet tails, including fascin, fimbrin, alpha-actinin, and filamin (8, 15, 18–20). Our data provide unique insight at the molecular level into the local environment of actin networks where these proteins are known to act. The interfilament angular range we found is in good agreement with the geometries induced in actin filaments by these proteins, which are known to vary in cross-bridge conformations, angles, stoichiometry, and lengths, as well as in the relative rotation and axial offset between neighboring filaments (21–23). Moreover, the spacings between the filaments are consistent with fimbrin cross-linking spacings of 11.5–12 nm (23) but far from spacings reported for fascin (8–9 nm) (24) or alpha-actinin (39 nm) (25).

In addition, our analysis unveiled long-range order in the structures. In our actin-tail data, two of the protrusions exhibited a second-order peak (i.e., reflecting distances at a position corresponding to twice the main interfilament spacing) (Fig. 2D). We did not detect significant contributions of filaments with an angular orientation of 70° in cytoplasmic comet tails (Fig. 1D and

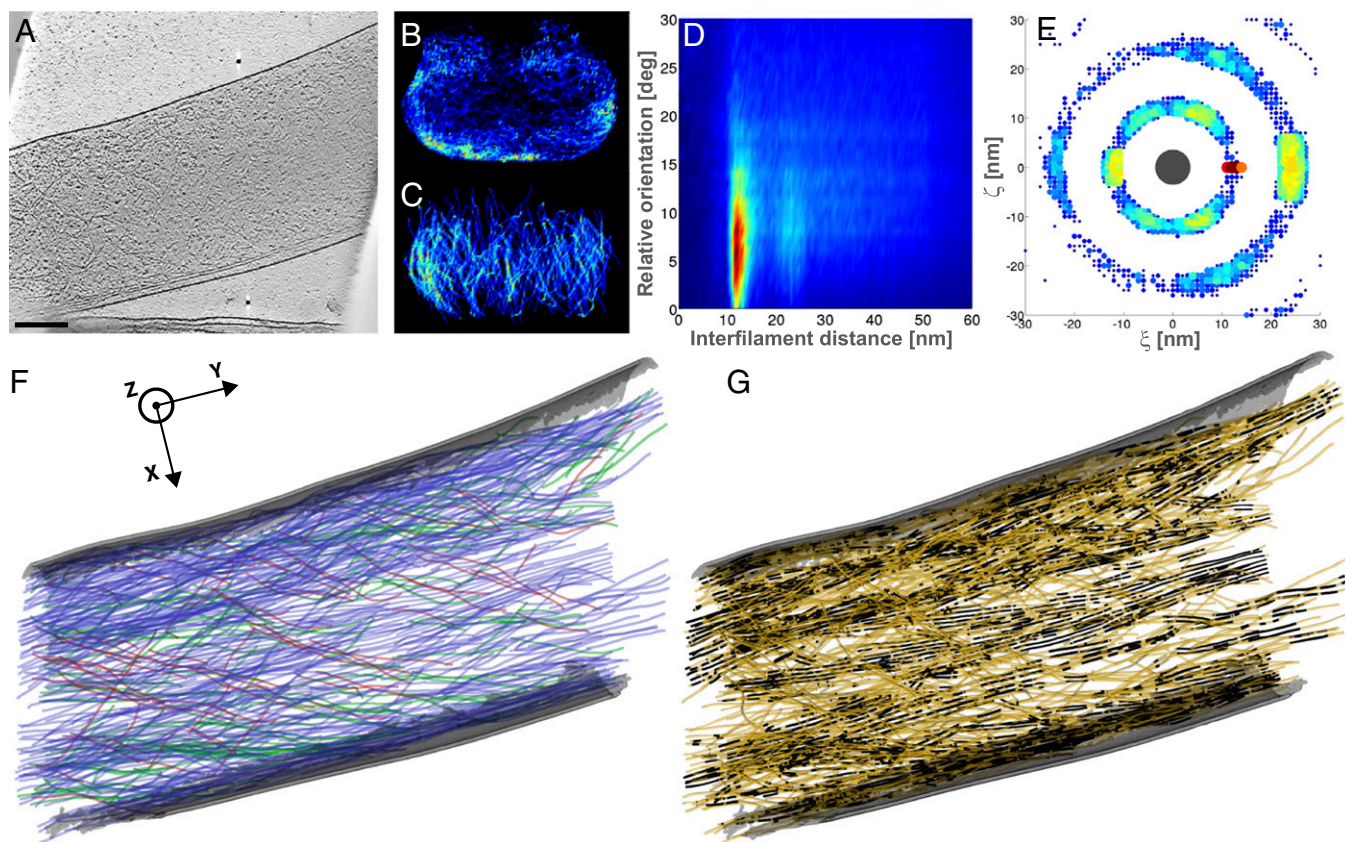


Fig. 2. *Listeria* protrusion shows hexagonal bundles in the vicinity of the plasma membrane. (A) Slice through the tomogram of a protrusion formed by *Listeria* at the surface of a PtK2 cell. The electron micrograph is shown in Fig. S3A. (Scale bar: 200 nm.) Distribution of XY-filaments (B) and Z-filaments (C) in the XZ plane, projected over the Y axis. (D) Two-dimensional histogram of interfilament distances, weighted by the distance, and relative orientations between the filaments. (E) Two-dimensional histogram of the (ξ , ζ) coordinates of the neighboring filaments in an XY-bundle in the local plane perpendicular to the central filament (dark gray, drawn to scale). (F) XY-filaments projected into the XY plane (same color code as in Fig. 1F). The plasma membrane of the protrusion is shown in gray. (G) XY-pairs of parallel filaments (black) among XY-filaments (orange).

Figs. S1D and S2D) or in protrusions (Fig. S4 K and M). This suggests that branches within the actin comet tails either escape detection or are rather short, and therefore likely to be excluded during the elimination of small filaments.

Filopodia and Stress Fibers Show Similar Interfilament Spacings as Found in Comet Tails. Filopodia are thin plasma membrane protrusions, in which actin is mainly bundled by fascin (26) (Fig. 3A and Fig. S6 A and F). Stress fibers are contractile actomyosin bundles mainly cross-linked by periodically arranged alpha-actinin (27) and possibly by other bundling proteins (Fig. 3C and Fig. S5 A and D). The actin filaments in the tomograms of stress fibers and filopodia were subjected to the same segmentation procedure and analysis. For interfilament angles between 0° and 15° , we found interfilament spacings of 12.2 ± 0.9 nm in filopodia (Fig. 3E and Fig. S6 D and I; four tomograms) and 13.3 ± 1.3 nm in stress fibers (Fig. 3G and Fig. S5 G and I; eight tomograms). Strikingly, *Listeria* cytoplasmic comet tails and protrusions, as well as filopodia and stress fibers, all contain tightly packed parallel filaments of similar spacings. These spacings are in disagreement with those reported for fascin (24) or alpha-actinin (25) in vitro.

In one filopodium network, second- and third-order peaks were detected (Fig. 3E), reflecting long-range order. In stress fibers, a second-order peak was detectable among contributions of spacings over the full distance range (Fig. 3G and Fig. S5 G and I). This indicates that although longer range order exists, parallel filaments are less ordered in stress fibers than in filopodia.

Actin Packing in Comet Tails, Filopodia, and Stress Fibers. We investigated the proportion of parallel filaments for each type of actin network (SI Text and Table S1). We define pairs as being composed of two parallel filament segments, bundles as being built of at least three parallel filament segments, and sheets as planar bundles (i.e., made of three parallel filament segments in the same plane). Parallel filaments were absent from Z-filaments. The percentage of pairs among XY-filaments (“XY-pairs”) is up to 21% in cytoplasmic tails (Fig. 1G, Figs. S1F and S2G, and Table S1), 35% in protrusions (Fig. 2G and Figs. S3E and S4 I and J), 63% in stress fibers (Fig. 3D and Fig. S5 C and F), and 72% in filopodia (Fig. 3B and Fig. S6 C and H). Sheets found among XY-filaments (“XY-sheets”) were almost absent from cytoplasmic comet tails (<2%), rare in protrusions (1–7%) and in stress fibers (6–16%), but more abundant in filopodia (12–25%). We explored further the order of packing of parallel XY-filaments. We looked for filament packing in a hexagonal lattice (“XY-hexagonal bundle”) (SI Text). Less than 1% fell into that category in cytoplasmic comet tails, up to 6% in protrusions, between 3 and 14% in stress fibers, and between 9 and 30% in filopodia. Filopodia appear to have the highest long-range order in the spatial arrangement of the filaments.

Filopodia Form Hexagonal Bundles, Whereas Stress Fibers Organize in Sheets. To distinguish between sheets and hexagonal packing, we examined the spatial distribution of XY-filaments belonging to a bundle (“XY-bundle”) (SI Text and Fig. S8G).

Filopodia were typically between 100 and 150 nm in diameter (Fig. 3A and Fig. S6 A and F). Two filopodia networks contain

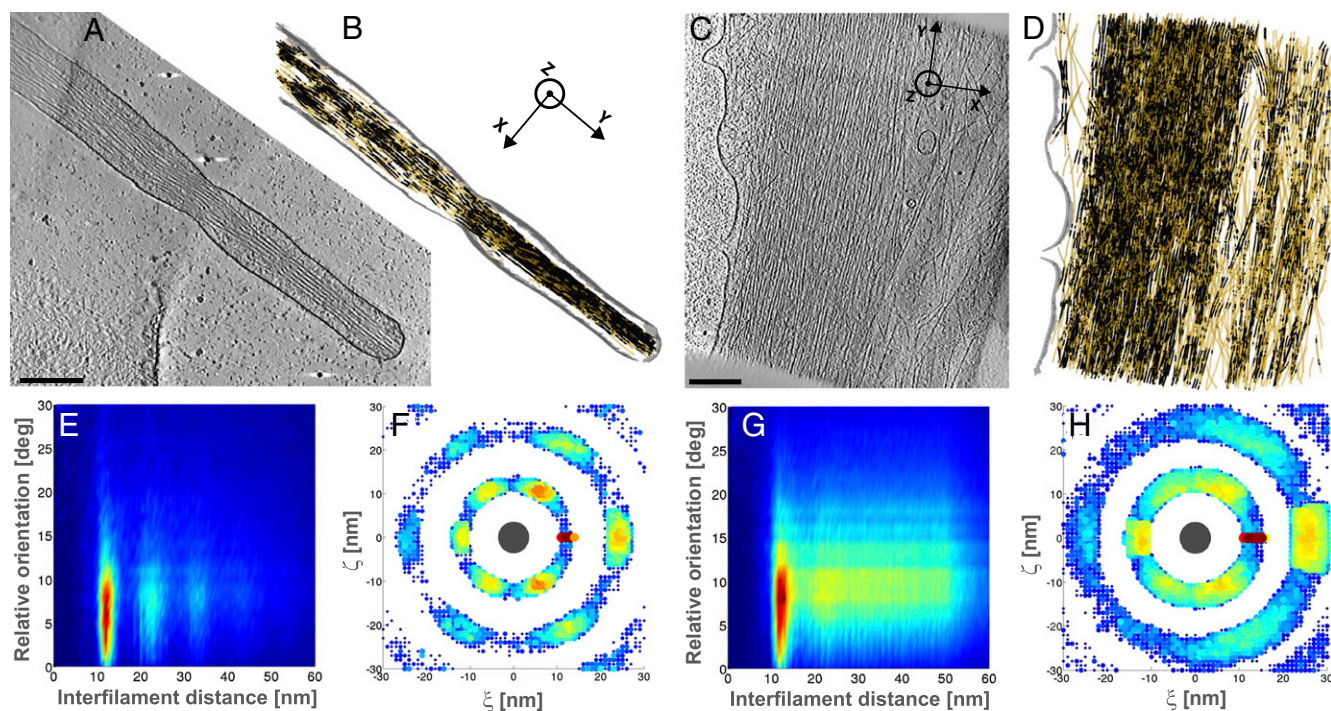


Fig. 3. Filopodia and stress fibers contain hexagonal bundles. Slices through the tomograms of a filopodium (A) and a stress fiber (C) of a PtK2 cell. (Scale bar: 200 nm.) (B and D) XY-pairs of parallel filaments (black) among XY-filaments (orange). The plasma membrane is shown in gray. (E and G) Two-dimensional histogram of interfilament distances, weighted by the distance, and relative orientations between the filaments. (F and H) Two-dimensional histogram of the (ξ , ζ) coordinates of the neighboring filaments in an XY-bundle in the local plane perpendicular to the central filament (dark gray, drawn to scale).

hexagonal close-packed XY-bundles made of two to three layers, with up to 36 rotationally arranged neighboring filaments and a mean spacing of 12.2 nm (Fig. 3F, Fig. S6E, and Table S1). The other two filopodia are less tightly packed but also contain hexagonal bundles (Fig. S6F). Our data imply that filopodia are made of large bundles comprising six to eight layers, hexagonally packed locally but with some imperfections in the overall packing.

Stress fibers comprise stacked XY-sheets containing laterally up to five filaments with a mean spacing of 13.3 nm (Fig. 3H and Fig. S5 H and J). The full range of interfilament spacings found in stress fibers (Fig. 3G and Fig. S5 G and I) indicates that on a larger length scale, they form less regular and densely packed XY-sheets. This looser overall packing would allow for the stress fibers to fulfill their contractile role, providing flexibility to the network. This is also consistent with the alternation of filament polarity reported in PtK2 cells at a typical periodicity of 0.6 μ m along the filament length (28), which may induce irregularities in the filament distribution through the network.

Protrusions Are Built of Hexagonal Bundles Adjacent to the Plasma Membrane. Most of the protrusions (Fig. S4 L and N; seven of nine tomograms) and all cytoplasmic comet tails (Fig. 1E and Fig. S2E; five tomograms) contain XY-pairs or XY-sheets of up to four filaments. In some protrusions, stacked XY-sheets were also visible (Fig. S4L). Protrusions tend to have higher local order than cytoplasmic comet tails. In two of them, we observed hexagonal close-packed XY-bundles (made of two layers) (Fig. 2E and Fig. S3D) in the vicinity of the plasma membrane (Fig. 2B). Interestingly, reconstituted lipid bilayers are known to be capable of inducing filopodium-like protrusions from branched actin networks without the help of bundling or tip-complex proteins (29). Our data indicate that, in situ, in protrusions assembled by *Listeria*, bundle formation is favored in the vicinity of the plasma membrane. This is likely due to interactions between actin and the plasma membrane, which have been ascribed to

ezrin, a protein that accumulates at the plasma membrane of the protrusions (3) and contributes to their formation (30).

Discussion

Actin Clouds Are Made of Z-Filaments, Which Serve to Nucleate XY-Filaments. The tangential orientation of both Z- and XY-filaments with respect to the bacterial cell wall is likely to arise from a favored nucleation pattern. It has been shown that nucleation geometry can be the principal determinant of actin-network architecture (31). The bacterial surface protein ActA serves to nucleate actin assembly, together with the Arp2/3 complex (9, 10). Arp2/3 nucleates daughter filaments, creating branches from preexisting filaments (10–12). Filaments parallel to a surface have been proposed to favor branching along it (32). Our data on actin clouds at the earliest stage in the comet tail assembly show that clouds are mostly made of short Z-filaments (Fig. 4C and Fig. S10), indicating that Z-filaments are nucleated first, and thus are likely to serve as preexisting filaments for new branches along the bacterial surface. The orientation of XY-filaments with respect to Z-filaments is compatible with a branch junction (Fig. 4A). ActA, together with Arp2/3, could therefore generate branches from Z-filaments, resulting in the nucleation of XY-filaments. Furthermore, the hexagonally packed XY-filaments detected in our data explain the maximum packing density of 0.3 ActA molecules per 100 nm² measured at the *Listeria* surface and found to be compatible with a hexagonal lattice constant of 11.4 nm (33).

Similar Interfilament Spacings Are Observed with a Variety of Bundlers. Filopodia have a mean interfilament spacing of 12.2 nm (Table S1) and exhibit hexagonal packing, suggesting that fascin, the dominant bundling protein in filopodia (26), enables this geometry. Protrusions are mainly bundled by fascin and fimbrin (8, 18, 20), resulting in a mean interfilament spacing of 12.3 nm. This value is in agreement with in vitro work on 2D actin arrays cross-linked by fimbrin (23) and with our filopodia data. Alpha-actinin, which is absent from protrusions (3), is one of the main

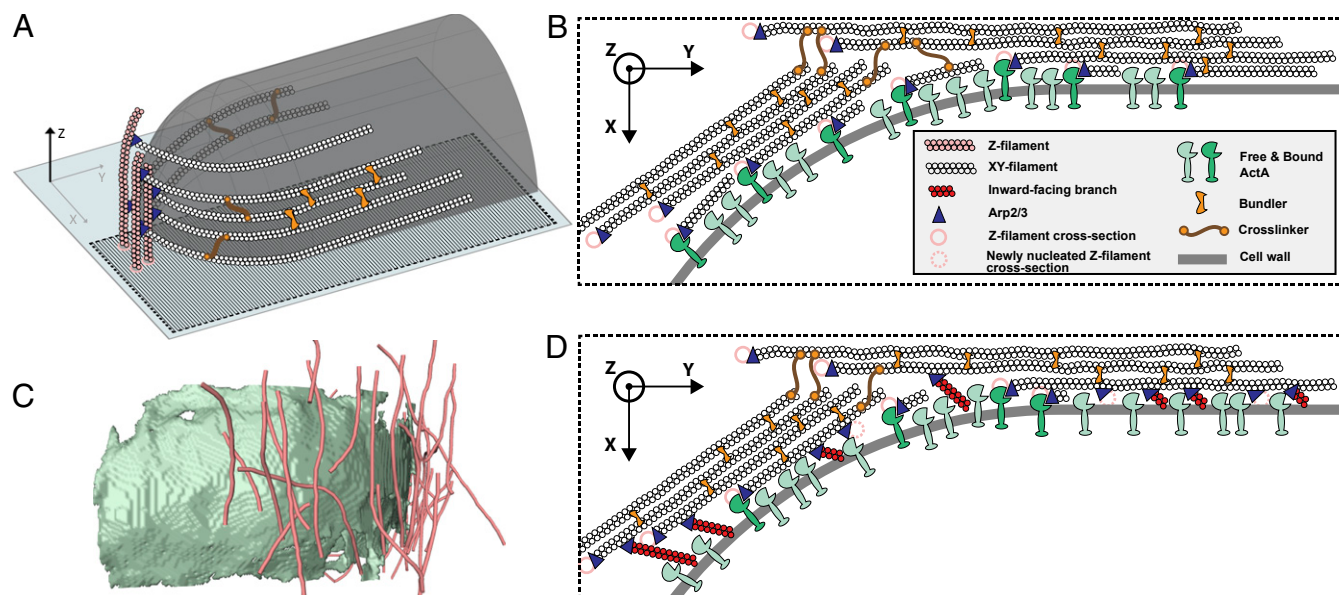


Fig. 4. Mechanism for the initiation of comet tail assembly and scenarios for *Listeria* actin-based propulsion. (A) Z-filaments (pink) are first nucleated tangentially to the bacterial cell wall (transparent gray). XY-filaments (white) originate as branches from Z-filaments, which act as “primers” (32) for XY-filament growth tangential to the cell wall in the XY plane. (B) Model of squeezing bundles. The de novo nucleation of XY-filaments along the bacterial surface, constrained to grow between the surface and the stiff scaffold of cross-linked XY-bundles, creates a squeezing stress, which pushes the bacterium forward. (C) Side view of Z-filaments (pink) extracted from the tomogram of an actin cloud (Fig. S10). The cell wall of the bacterium is shown in green. (D) Model of pushing bundles. The tangential orientation of the XY-bundles along the bacterial surface could favor Arp2/3-dependent explosive growth of branches at the surface, as proposed by Achard et al. (32). Tangential branches from XY-filaments could give rise to newly nucleated Z-filaments (dashed pink circles). Inward- and outward-facing branches are not displayed here. The simultaneous polymerization of these multiple branches, constrained to grow between the surface and the stiff scaffold of cross-linked XY-bundles, could generate a compressive stress, which pushes the bacterium forward.

cross-linkers in cytoplasmic comet tails (15) and in stress fibers (27). Our data suggest further that alpha-actinin, mostly known as a cross-linker, can contribute to bundling and give rise to a mean interfilament spacing between 12.8 and 13.3 nm (Table S1); alpha-actinin appears to favor an arrangement in sheets. Different bundling proteins, despite differences in cross-bridge conformation, angles, and length, apparently satisfy a narrow range of interfilament spacings. Moreover, most of the network architectures we observed, and thus most or all of the bundling proteins involved, allow for hexagonal packing.

Actin Comet Tails in Situ Contain Stiff, Cross-Linked Bundles. The established presence of alpha-actinin or filamin in the comet-tail networks (15, 19) implies that the XY-bundles are cross-linked to some extent. *Listeria* comet tails would therefore consist of interconnected bundles that cover the rear end of the bacteria. An actin bundle was found to be two orders of magnitude stiffer than a group of non-cross-linked actin filaments of similar radius (34). Furthermore, compact bundles embedded into cross-linked orthogonal networks form significantly stiffer structures than structures containing only bundles or only orthogonally cross-linked individual filaments (35). Based on our observation of actin bundling in comet tails, we predict that *Listeria* assembles stiffer structures than previously suggested (1, 2).

Cross-Linked Actin Bundles Can Provide the Stiffness Necessary for Intracellular Movement and Cell-to-Cell Spread. The mechanism of force generation in *Listeria* motility is still under debate. It has been analyzed extensively using experimental biomimetic systems (36), combined with theoretical models on both molecular and mesoscopic scales (37). In vitro assays rely on functionalized latex beads or lipid vesicles, as well as reconstituted motility medium (38) or cell extracts. A branched (so-called “dendritic”) organization has been observed in comet tails at the surface of latex beads in cell extracts (39). Based on this observation and aiming toward the reconstitution of actin-based motility directly

from essential proteins, in vitro studies have not taken into account the role of filament bundling in the force generation mechanism. Here, we show that the 3D architecture of *Listeria* comet tails differs from a dendritic organization. Moreover, bundling proteins, which are not included in the minimal set of proteins reported to generate actin-based motility (38), are nevertheless likely to play an important role in *Listeria* motility. It is probable that *Listeria* movement in the crowded cellular environment requires a higher force to push the bacteria forward than in biomimetic motility systems. The combination of local bundling of the actin filaments and overall cross-linking of the actin bundles could provide the necessary stiffness. In protrusions, the higher order of packing at the membrane could increase the efficiency of force transmission along a particular direction and appears to be a general mechanism of cellular protrusions.

Initiation of Comet Tail Assembly. We propose the following mechanism for the initiation of *Listeria* comet tail assembly, based on our experimental data and recent in vitro work on branch formation initiated by tangential filaments (“primers”) to a surface (32). Z-filaments are nucleated first at the bacterial surface. They could possibly be nucleated through ActA and Arp2/3 as branches from surrounding cytoskeletal filaments in the vicinity of the *Listeria* cell wall. XY-filaments originate as branches from Z-filaments, which act as primers (32) for the growth of XY-filaments (Fig. 4A). XY-filaments are densely nucleated due to the close packing of ActA at the bacterial surface, possibly already in an arrangement compatible with hexagonal packing. The various bundling proteins in comet tails promote hexagonal packing. The XY-bundles could be cross-linked over the entire comet tail, and in the case of protrusions, they are supported by and anchored to the plasma membrane, probably by the membrane linker ezrin. The comet tail therefore consists of a stiff scaffold of interconnected bundles at the rear end of the bacteria.

Scenarios for Intracellular Movement and Cell-to-Cell Spread: Squeezing Bundles vs. Pushing Bundles. Once the comet tail is longer than the bacteria, *Listeria* can move while the comet tail remains stationary (36). This takes place due to the viscous force that opposes the motion of an object in the cytoplasm and increases as a function of the object size. The two following scenarios can occur either independently or in concert, enabling *Listeria* motility. In a first scenario, the de novo nucleation of XY-filaments along the bacterial surface, constrained to grow between the surface and the stiff scaffold of cross-linked XY-bundles, creates a squeezing stress that pushes the bacterium forward (Fig. 4B). This nanoscopic model of “squeezing bundles” supports the mesoscopic “elastic propulsion” model, where the comet tail is seen as an elastic gel that generates squeezing forces (36, 40, 41). In a second scenario (“pushing bundles”) (Fig. 4D), the tangential orientation of the de novo XY-filaments along the bacterial surface, part of XY-bundles, can favor an Arp2/3-dependent explosive growth of branches at the surface, as proposed by Achard et al. (32). These small branches, which may have been removed from the analysis, can grow toward (“inward-facing branches”), tangentially to (“tangential branches”), or away from (“outward-facing branches”) the surface. Tangential branches from XY-filaments can give rise to newly nucleated Z-filaments. Inward-facing branches have been proposed to be stalled by the surface until they escape and grow tangentially as well, whereas outward-facing branches were found to be capped rapidly (32). Here, we propose that the simultaneous polymerization of multiple tangential, inward- and outward-facing

branches constrained to grow between the surface and the stiff scaffold of XY-bundles can generate a compressive stress, which results in the bacterial motion. This process gives rise to new Z-filaments, which, in turn, allow for de novo polymerization of XY-filaments.

Materials and Methods

Detailed experimental procedures and references are given in *SI Text*. Briefly, cells were grown on EM grids and used for the infection assays, followed by cryofixation. CET was performed using a Tecnai G2 Polara transmission electron microscope (FEI). Tilt series were recorded with SerialEM, and tomograms were calculated using IMOD. Tomograms were then subjected to template matching using the filament segmentation package in Amira (FEI). Data analysis was performed in MATLAB (MathWorks) using as input the coordinates of the automatically detected filaments. The analysis is described in detail in *SI Text*.

ACKNOWLEDGMENTS. We thank D. Günther and A. Rigort for help with the Amira software; A. Martinez-Sanchez for help with the membrane segmentation of the *Listeria* cell wall; S. Mostowy, A. H. Crevenna, L. F. Kourkoutis, and M. Schüler for fruitful discussions; and G. Gerisch for critical reading of the manuscript. This work was supported by a European Molecular Biology Organization Long-Term Fellowship and a Marie Curie Action Intra-European Fellowship (to M.J.), the European Research Council (Grant 233348, to P.C.), European Union Seventh Framework Program Proteomics Specification in Space and Time Grant HEALTH-F4-2008-201648 (to W.B.), Deutsche Forschungsgemeinschaft Excellence Cluster Center for Integrated Protein Science Munich Grant GRK 1721 (to E.V.), the Federal Ministry of Education and Research, and an interinstitutional research initiative of the Max Planck Society.

1. Tilney LG, Portnoy DA (1989) Actin filaments and the growth, movement, and spread of the intracellular bacterial parasite, *Listeria monocytogenes*. *J Cell Biol* 109(4 Pt 1):1597–1608.
2. Gouin E, et al. (1999) A comparative study of the actin-based motilities of the pathogenic bacteria *Listeria monocytogenes*, *Shigella flexneri* and *Rickettsia conorii*. *J Cell Sci* 112(Pt 11):1697–1708.
3. Sechi AS, Wehland J, Small JV (1997) The isolated comet tail pseudopodium of *Listeria monocytogenes*: A tail of two actin filament populations, long and axial and short and random. *J Cell Biol* 137(1):155–167.
4. Tilney LG, Connelly PS, Portnoy DA (1990) Actin filament nucleation by the bacterial pathogen, *Listeria monocytogenes*. *J Cell Biol* 111(6 Pt 2):2979–2988.
5. Tilney LG, DeRosier DJ, Tilney MS (1992) How *Listeria* exploits host cell actin to form its own cytoskeleton. I. Formation of a tail and how that tail might be involved in movement. *J Cell Biol* 118(1):71–81.
6. Tilney LG, DeRosier DJ, Weber A, Tilney MS (1992) How *Listeria* exploits host cell actin to form its own cytoskeleton. II. Nucleation, actin filament polarity, filament assembly, and evidence for a pointed end capper. *J Cell Biol* 118(1):83–93.
7. Zhukarev V, Ashton F, Sanger JM, Sanger JW, Shuman H (1995) Organization and structure of actin filament bundles in *Listeria*-infected cells. *Cell Motil Cytoskeleton* 30(3):229–246.
8. Briehner WM, Coughlin M, Mitchison TJ (2004) Fascin-mediated propulsion of *Listeria monocytogenes* independent of frequent nucleation by the Arp2/3 complex. *J Cell Biol* 165(2):233–242.
9. Welch MD, Iwamatsu A, Mitchison TJ (1997) Actin polymerization is induced by Arp2/3 protein complex at the surface of *Listeria monocytogenes*. *Nature* 385(6613):265–269.
10. Welch MD, Rosenblatt J, Skoble J, Portnoy DA, Mitchison TJ (1998) Interaction of human Arp2/3 complex and the *Listeria monocytogenes* ActA protein in actin filament nucleation. *Science* 281(5373):105–108.
11. Amann KJ, Pollard TD (2001) Direct real-time observation of actin filament branching mediated by Arp2/3 complex using total internal reflection fluorescence microscopy. *Proc Natl Acad Sci USA* 98(26):15009–15013.
12. Mullins RD, Heuser JA, Pollard TD (1998) The interaction of Arp2/3 complex with actin: Nucleation, high affinity pointed end capping, and formation of branching networks of filaments. *Proc Natl Acad Sci USA* 95(11):6181–6186.
13. Lucić V, Förster F, Baumeister W (2005) Structural studies by electron tomography: From cells to molecules. *Annu Rev Biochem* 74:833–865.
14. Rigort A, et al. (2012) Automated segmentation of electron tomograms for a quantitative description of actin filament networks. *J Struct Biol* 177(1):135–144.
15. Dabiri GA, Sanger JM, Portnoy DA, Southwick FS (1990) *Listeria monocytogenes* moves rapidly through the host-cell cytoplasm by inducing directional actin assembly. *Proc Natl Acad Sci USA* 87(16):6068–6072.
16. Theriot JA, Mitchison TJ, Tilney LG, Portnoy DA (1992) The rate of actin-based motility of intracellular *Listeria monocytogenes* equals the rate of actin polymerization. *Nature* 357(6375):257–260.
17. Sanger JM, Sanger JW, Southwick FS (1992) Host cell actin assembly is necessary and likely to provide the propulsive force for intracellular movement of *Listeria monocytogenes*. *Infect Immun* 60(9):3609–3619.
18. Kocks C, Cossart P (1993) Directional actin assembly by *Listeria monocytogenes* at the site of polar surface expression of the actA gene product involving the actin-bundling protein plastrin (fimbrin). *Infect Agents Dis* 2(4):207–209.
19. Van Kirk LS, Hayes SF, Heinzen RA (2000) Ultrastructure of *Rickettsia rickettsii* actin tails and localization of cytoskeletal proteins. *Infect Immun* 68(8):4706–4713.
20. Van Troys M, et al. (2008) The actin propulsive machinery: The proteome of *Listeria monocytogenes* tails. *Biochem Biophys Res Commun* 375(2):194–199.
21. Hampton CM, Taylor DW, Taylor KA (2007) Novel structures for alpha-actinin:F-actin interactions and their implications for actin-membrane attachment and tension sensing in the cytoskeleton. *J Mol Biol* 368(1):92–104.
22. Hanein D, et al. (1998) An atomic model of fimbrin binding to F-actin and its implications for filament crosslinking and regulation. *Nat Struct Biol* 5(9):787–792.
23. Volkmann N, DeRosier D, Matsudaira P, Hanein D (2001) An atomic model of actin filaments cross-linked by fimbrin and its implications for bundle assembly and function. *J Cell Biol* 153(5):947–956.
24. Ishikawa R, Sakamoto T, Ando T, Higashi-Fujime S, Kohama K (2003) Polarized actin bundles formed by human fascin-1: Their sliding and disassembly on myosin II and myosin V in vitro. *J Neurochem* 87(3):676–685.
25. Taylor KA, Taylor DW, Schachar F (2000) Isoforms of alpha-actinin from cardiac, smooth, and skeletal muscle form polar arrays of actin filaments. *J Cell Biol* 149(3):635–646.
26. DeRosier DJ, Edds KT (1980) Evidence for fascin cross-links between the actin filaments in coelomocyte filopodia. *Exp Cell Res* 126(2):490–494.
27. Lazarides E, Burridge K (1975) Alpha-actinin: Immunofluorescent localization of a muscle structural protein in nonmuscle cells. *Cell* 6(3):289–298.
28. Cramer LP, Siebert M, Mitchison TJ (1997) Identification of novel graded polarity actin filament bundles in locomoting heart fibroblasts: Implications for the generation of motile force. *J Cell Biol* 136(6):1287–1305.
29. Liu AP, et al. (2008) Membrane-induced bundling of actin filaments. *Nat Phys* 4:789–793.
30. Pust S, Morrison H, Wehland J, Sechi AS, Herrlich P (2005) *Listeria monocytogenes* exploits ERM protein functions to efficiently spread from cell to cell. *EMBO J* 24(6):1287–1300.
31. Reymann AC, et al. (2010) Nucleation geometry governs ordered actin networks structures. *Nat Mater* 9(10):827–832.
32. Achard V, et al. (2010) A “primer”-based mechanism underlies branched actin filament network formation and motility. *Curr Biol* 20(5):423–428.
33. Footer MJ, Lyo JK, Theriot JA (2008) Close packing of *Listeria monocytogenes* ActA, a natively unfolded protein, enhances F-actin assembly without dimerization. *J Biol Chem* 283(35):23852–23862.
34. Shin JH, Mahadevan L, So PT, Matsudaira P (2004) Bending stiffness of a crystalline actin bundle. *J Mol Biol* 337(2):255–261.
35. Wirtz D, Khatauo SB (2010) Protein filaments: Bundles from boundaries. *Nat Mater* 9(10):788–790.
36. Plastino J, Sykes C (2005) The actin slingshot. *Curr Opin Cell Biol* 17(1):62–66.
37. Mogilner A (2006) On the edge: Modeling protrusion. *Curr Opin Cell Biol* 18(1):32–39.
38. Loisel TP, Boujemaa R, Pantaloni D, Carlier MF (1999) Reconstitution of actin-based motility of *Listeria* and *Shigella* using pure proteins. *Nature* 401(6753):613–616.
39. Cameron LA, Svitkina TM, Vignjevic D, Theriot JA, Borisy GG (2001) Dendritic organization of actin comet tails. *Curr Biol* 11(2):130–135.
40. Gerbal F, Chaikin P, Rabin Y, Prost J (2000) An elastic analysis of *Listeria monocytogenes* propulsion. *Biophys J* 79(5):2259–2275.
41. Bernheim-Groswasser A, Prost J, Sykes C (2005) Mechanism of actin-based motility: A dynamic state diagram. *Biophys J* 89(2):1411–1419.

Supporting Information

Jasnin et al. 10.1073/pnas.1320155110

SI Text

Bacterial Strains, Mammalian Cells, and Culture Conditions. *Listeria monocytogenes* strain EGD (BUG 600) was grown overnight at 37 °C in brain heart infusion (BHI) media (Difco Laboratories), diluted 10-fold in fresh BHI, and cultured until $OD_{600} = 0.8$. *L. monocytogenes* EGD-cGFP (BUG 2539) and L028 (BUG 666) were similarly grown, except that media contained 5 μ g/mL chloramphenicol. Potoroo kidney epithelial Ptk2 (American Type Culture Collection CCL56) cells were cultured in MEM plus GlutaMAX (GIBCO) supplemented with 1 mM sodium pyruvate (GIBCO), 0.1 mM nonessential amino acid solution (GIBCO), and 10% (vol/vol) FBS. Ptk2 cells were grown at 37 °C and 10% (vol/vol) CO_2 .

Infections and Cryopreparation. Holey carbon film-coated gold EM grids (C-flat 2/1-2Au; Protochips, Inc.) were glow-discharged and sterilized on 35-mm diameter Petri dishes under UV light for 15 min. The grids were incubated in MEM at 37 °C and 10% CO_2 for a few hours and then rinsed with fresh medium. Ptk2 cells were then plated on the grids and used 48 h later for the infection assays. *Listeria* was added to host cells at a multiplicity of infection of 10. Infected cells were grown at 37 °C and 10% CO_2 for 2 h, washed with MEM, and incubated with fresh medium for an additional 2 or 3 h. For cryopreparation, we added 15-nm BSA coated colloidal gold on top of the grids, removed excess liquid by blotting from the reverse side, and rapidly plunge-froze the grids in a liquid propane-ethane mixture.

Cryo-Electron Tomography. Cryo-electron tomography (CET) was performed under low-dose conditions using a Tecnai G2 Polara transmission electron microscope (FEI) equipped with a 300-kV field emission gun, a Gatan GIF 2002 postcolumn energy filter, and a 2,048 \times 2,048 slow-scan CCD camera (Gatan). The electron microscope was operated at an accelerating voltage of 300 kV, and the pixel size at the specimen level was 0.713 nm. Tilt series were recorded using SerialEM software (1), typically covering an angular range from -55° to $+55^\circ$ with a tilt increment of 1.5° , a defocus of -12μ m, and a total electron dose of 200 electrons per \AA^2 . The applied electron dose for a given tilt angle α was proportional to $1/\cos(\alpha)$ to compensate for the higher effective specimen thickness at high tilts. The projection images were aligned using the gold beads as fiducial markers. Three-dimensional reconstructions (tomograms) with one time-binned pixel size of 1.42 nm were calculated using IMOD software (2).

Automated Filament Segmentation. We applied an automated segmentation algorithm developed for the tracking of actin filaments, using a generic filament as a template (3). This method can detect filaments in every orientation, including filaments that are parallel to the imaging direction, and thus appear as small cross-sectional spots in a given slice. Tomograms were first subjected to nonlocal means filtering (Fig. S8A) and then to template matching using the filament segmentation package implemented in Amira software (FEI) (4). The diameter and length of the cylindrical template were 8 nm and 42 nm, respectively. From the resulting correlation and orientation field maps [more details are provided in the study by Rigort et al. (3)], a similarity function, which evaluates the likelihood that two neighboring voxels belong to the same filament, was calculated. Filaments were traced using threshold correlation values ranging from 0.3 to 0.62, adjusted for each tomogram to provide reliable networks

(Fig. S8B). Short filaments (<100 nm in comet tails, <70 nm in stress fibers and filopodia) were filtered out to avoid false-negative results due to background noise. When present, the cell wall of the bacterium was extracted from the tomograms using the membrane segmentation method developed by Martinez-Sanchez et al. (5, 6).

Quantitative Data Analysis. Data analysis was performed in the computing platform MATLAB (MathWorks), using as input the coordinates of the automatically detected filaments exported from the Amira software as an ASCII file. The Amira package does not yield equidistant points along a filament [details are provided in the study by Rigort et al. (3)]. To perform the analysis giving the same weight to every point along a filament, the filaments were oversampled at 0.1-nm intervals using a linear interpolation, followed by an undersampling at 3-nm intervals, which is twice the pixel size and close to the Nyquist frequency. Fine sampling steps of 0.1 nm were found to provide the best fit to the original data. Varying final sampling distances between 1 and 4 nm did not affect the results significantly.

Data acquisition for CET is limited to thin areas of the cell. This restricts the movement of the bacteria to a plane, which gives rise to an inhomogeneity in the directions perpendicular to the long axis of the comet tail. Therefore, it was adequate to define the plane of the substrate as the frame of reference. Because the plane of the tomogram reconstruction may deviate from the substrate plane, we used principal component analysis on the coordinates of the resampled filaments to define the substrate plane as the XY plane. The first and the second components were combined such that the Y axis points along the length of the network. The third component defines the Z axis.

We distinguish between filaments that have an inclination smaller than 30° with respect to the XY plane (XY-filaments), which we consider to be included in the XY plane, and filaments with an inclination larger than 30° (Z-filaments). In cases where the motion of the bacterium is not subject to constraints, the definition of XY- and Z-filaments could be generalized to on-axis and off-axis filaments, where the axis is defined as the long axis (Y axis here) of the comet tail. We evaluated the distribution of both XY-filaments and Z-filaments in the XZ plane, projected over the Y axis, as shown in Fig. S8C, where the color scale ranges from high occurrence (red) to low occurrence (blue).

To perform nearest neighbor analysis, we determined the local direction of the actin filament at each point along a filament as the tangent of the filament at that point. For each point of a filament, we characterized the closest point of each neighboring filament (within a cube of edge length of 100 nm) by its distance, d (in nanometers), and its relative orientation, α (in degrees), with respect to the reference filament. We represented the occurrences of (d, α) by a 2D histogram (Fig S8D); the occurrences along the distance axis are weighted by the distance. The peak occurring at small α indicates the presence of equidistant and nearly parallel filaments.

The projection of the 2D histogram along α results in a histogram of the distances as shown in Fig. S9. Summing up all histograms, but separately for cytoplasmic comet tails, protrusions, stress fibers, and filopodia, provides better statistics to evaluate the mean spacing between parallel filaments for each type of network. We defined a distance range, corresponding to distances with a number of occurrences equal to or higher than 60% of the peak maximum associated with parallel filaments (Fig. S9). This range of spacings between parallel filaments varies

for each type of cellular structure (Table S1). We then evaluated the mean interfilament spacing and the SD in this range.

To explore the local packing of the actin filaments in the networks, we defined a local frame of reference (e_1 , e_2 , e_3) at every point along a filament. The basis is defined as follows: e_2 points in the direction of the actin filament (the tangent of the filament at that point), and e_1 points in the direction of the nearest neighbor. If there are several nearest neighbors at similar distance, we chose the neighbor in the vicinity of their center of mass. The e_3 frame of reference is defined as the cross-product of e_1 and e_2 . (ξ , η , ζ) are the coordinates of a neighbor position in (e_1 , e_2 , e_3). We aligned the local frames of reference (e_1 , e_2 , e_3) of all points along filaments and represented the occurrences of (ξ , ζ) in the e_1 - e_3 plane by a 2D histogram (Fig. S8E). The definition of e_1 as pointing in the direction of the nearest neighbor yields the red (high intensity) spots in sector III of Fig. S8E. Furthermore, it prevents the appearance of an artificial symmetry by ensuring that each neighbor contribution is statistically significant. The asymmetry between the right side (sectors I to V; Fig. S8H) and the left side (sectors VII to XI) emerges from finite networks that are not perfectly packed. In the plots shown in Fig. S8E, the size of a point is proportional to the number of occurrences in a logarithmic scale, which also defines a red (high occurrence) to blue (low occurrence) color scale.

Our analysis clearly shows that near neighbors tend to be equidistant and arranged into shells (Fig. S8D and E). To unveil further the high-order packing of the filaments, we defined three layers. Layer 1 (green; Fig. S8D, G, and H) corresponds to the range of spacings between parallel filaments evaluated previously (Table S1). Layer 2 (yellow) and layer 3 (red) correspond to twofold and threefold the range of layer 1, respectively. We selected neighbors in layer 1, with a relative orientation α below or equal to 15° with respect to the reference filament. Every point (filament segment) with at least one neighbor satisfying this condition was displayed in black using the Amira software (Fig. S8F), highlighting the localization of pairs of closely packed parallel filaments (XY-pairs; Table S1). It should be noted here that pairs were quantified and displayed among XY-filaments because they were absent from Z-filaments.

We defined a bundle as made of at least three parallel equidistant points (filament segments) and a sheet as a planar bundle (i.e., made of three parallel, equidistant filament segments in the same plane). The spatial arrangement of the filaments in a bundle was evaluated as follows. We looked for neighbors in the three

layers mentioned above, which belong to a sheet containing the central point (filament segment). The sheet can be of any orientation with respect to the XY plane. Fig. S8G shows the occurrences of (ξ , ζ) of the selected neighbors in the e_1 - e_3 plane, for every filament segment centered in (0, 0) (displayed in a gray, filled circle). The point size increases with the number of occurrences in a logarithmic scale, which also defines the color scale. We evaluated the percentage of XY-filaments that belong to a sheet (XY-sheets), as well as the percentage of hexagonally packed bundles (XY-hexagonal bundles) (Table S1). In the latter case, the filament packing, which is commensurate to a hexagonal lattice, was defined by looking for two neighboring filaments in layer 1, which form an equilateral mesh with the central filament segment.

Description of the Spatial Distribution Plots. We observed well-defined populated areas in sectors I, III, V, VII, IX, and XI in the first two to three layers for two filopodia networks (Fig. 3F and Fig. S6E; two of four tomograms). These filopodia contain up to 6 rotationally arranged neighboring filaments in the first layer, 12 in the second layer, and 18 in the third layer, which pack hexagonally (the number of neighboring XY-filaments are shown in Table S1). In the other two filopodia (Fig. S6J), the contribution in sector IX.1 is similar to the contribution in sectors I.1 and V.1 despite the asymmetry in intensity induced by the method, which indicates a stronger contribution of the neighbors on the sides of the central filament (sectors III and IX), rather than in the upper (sectors I and XI) and lower (sectors V and VII) levels. It corresponds to an elementary organization in sheets, followed by hexagonal packing.

In all stress fibers, we observed a stronger contribution of lateral neighbors (sectors III and IX; Fig. 3H and Fig. S5H and J; eight tomograms) (i.e., stress fibers contain sheets that are placed on top of each other). In some cases, these sheets are hexagonally packed.

Most of the protrusions (Fig. S4L and N; seven of nine tomograms) and all cytoplasmic comet tails (Fig. 1E and Fig. S2E; five tomograms) contain XY-filaments with lateral neighbors (sectors III and IX). In some cases, different (upper and lower) instances were also detected (sectors I and V). In addition, in two of the protrusions, we observed well-defined populated areas in layer 1 in sectors I, III, V, VII, IX, and XI (Fig. 2E and Fig. S3D), accounting for hexagonally packed bundles as found for two filopodia networks.

1. Mastrorade DN (2005) Automated electron microscope tomography using robust prediction of specimen movements. *J Struct Biol* 152(1):36–51.
2. Kremer JR, Mastrorade DN, McIntosh JR (1996) Computer visualization of three-dimensional image data using IMOD. *J Struct Biol* 116(1):71–76.
3. Rigort A, et al. (2012) Automated segmentation of electron tomograms for a quantitative description of actin filament networks. *J Struct Biol* 177(1):135–144.
4. Stalling D, Westerhoff M, Hege H-C (2005) Amira: A highly interactive system for visual data analysis. *Visualization Handbook*, eds Charles DH, Chris RJ (Elsevier, Butterworth-Heinemann, Burlington, MA), pp 749–767.
5. Martinez-Sanchez A, Garcia I, Fernandez JJ (2011) A differential structure approach to membrane segmentation in electron tomography. *J Struct Biol* 175(3):372–383.
6. Martinez-Sanchez A, Garcia I, Fernandez JJ (2013) A ridge-based framework for segmentation of 3D electron microscopy datasets. *J Struct Biol* 181(1):61–70.

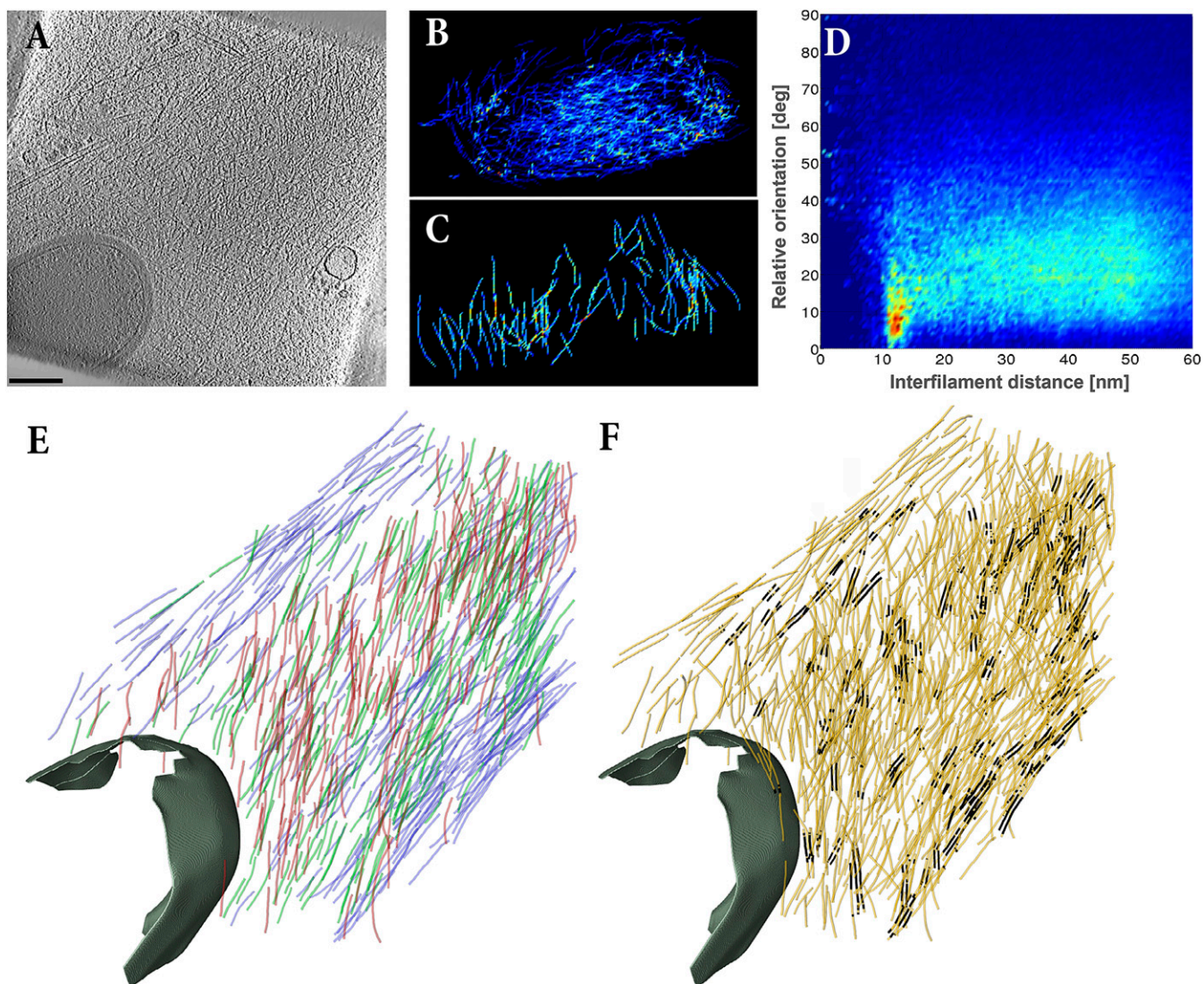


Fig. S1. Densely filled *Listeria* cytoplasmic comet tail contains closely packed parallel filaments. (A) Slice through the tomogram of a dense cytoplasmic comet tail in a PtK2 cell infected by *Listeria* EGD-cGFP. (Scale bar: 200 nm.) Distribution of XY-filaments (B) and Z-filaments (C) in the XZ plane, projected over the Y axis. (D) Two-dimensional histogram of interfilament distances, weighted by the distance, and relative orientations between the filaments. (E) XY-filaments projected into the XY plane. The color of the filaments corresponds to their angle with respect to the Y axis: 0–15° (blue), 15–30° (green), 30–45° (red). The cell wall of the bacterium is shown in gray. (F) XY-pairs of parallel filaments (black) among XY-filaments (orange).

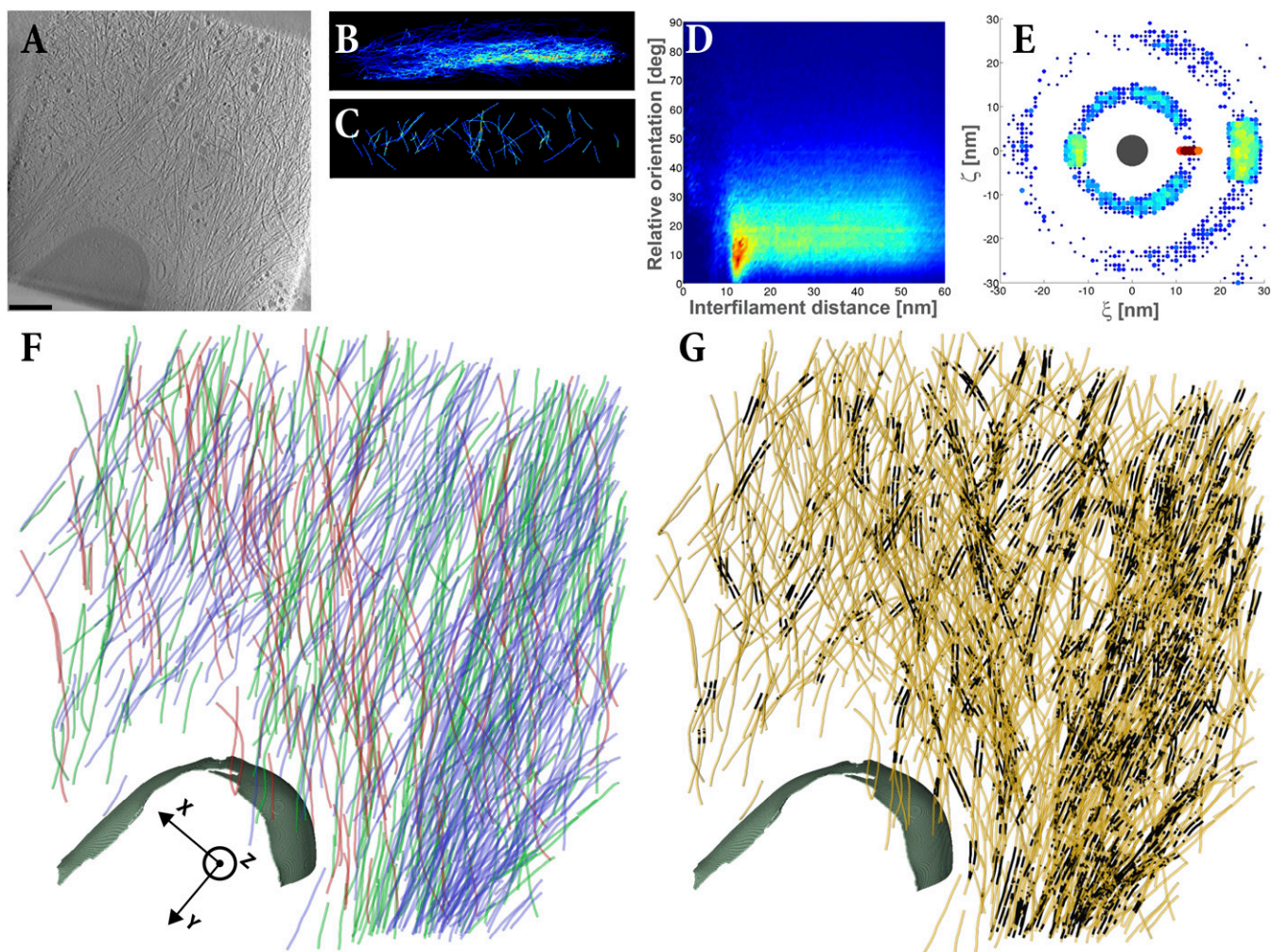


Fig. S2. Densely filled *Listeria* cytoplasmic comet tail shows tightly packed parallel filaments. (A) Slice through the tomogram of a dense cytoplasmic comet tail in a PtK2 cell infected by *Listeria* EGD-cGFP. (Scale bar: 200 nm.) Distribution of XY-filaments (B) and Z-filaments (C) in the XZ plane, projected over the Y axis. (D) Two-dimensional histogram of interfilament distances, weighted by the distance, and relative orientations between the filaments. (E) Two-dimensional histogram of the (ξ, ζ) coordinates of the neighboring filaments in an XY-bundle in the local plane perpendicular to the central filament (dark gray, drawn to scale). (F) XY-filaments projected into the XY plane using the same color code as in Fig. S1E. The cell wall of the bacterium is shown in gray. (G) XY-pairs of parallel filaments (black) among XY-filaments (orange).

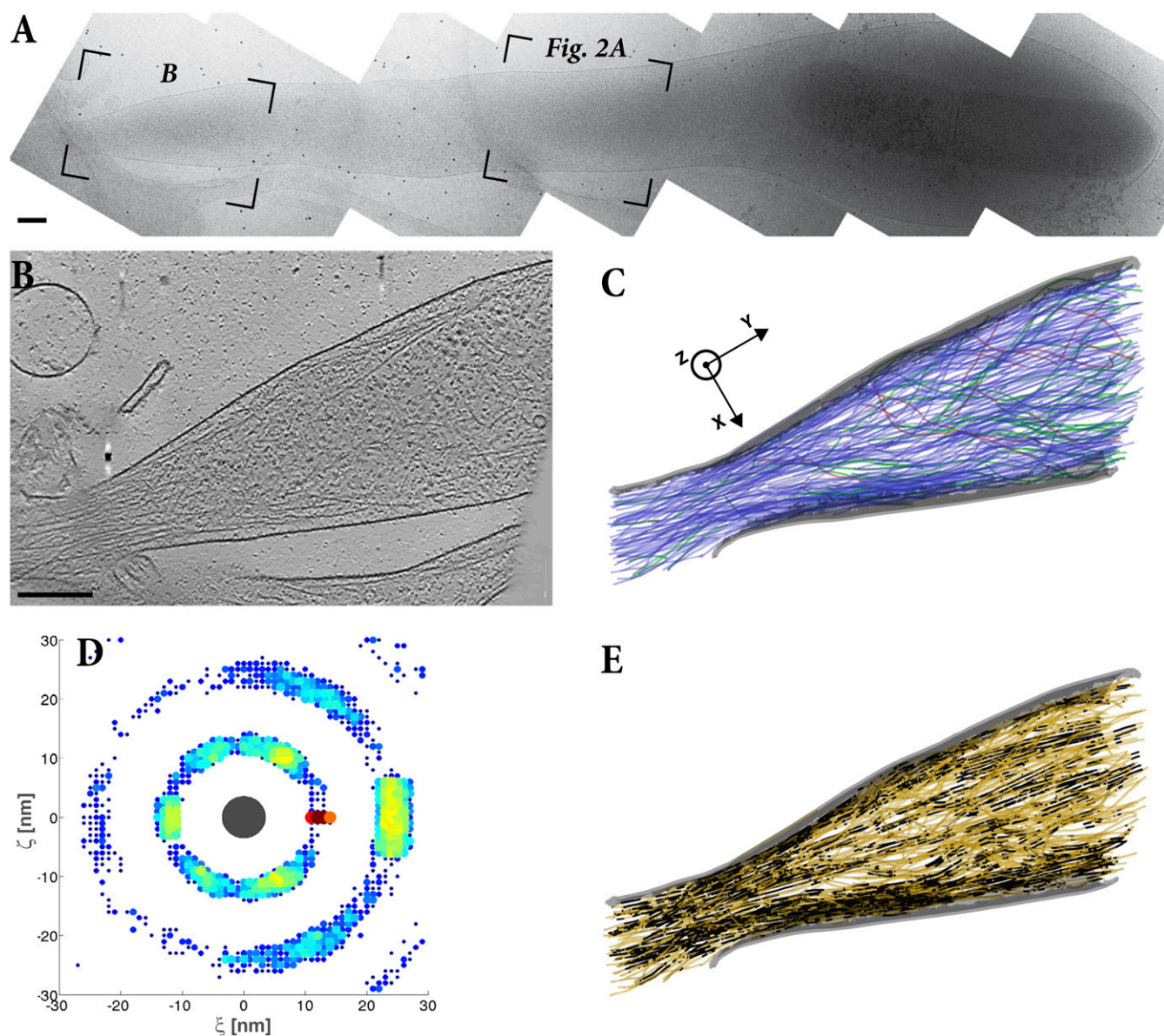
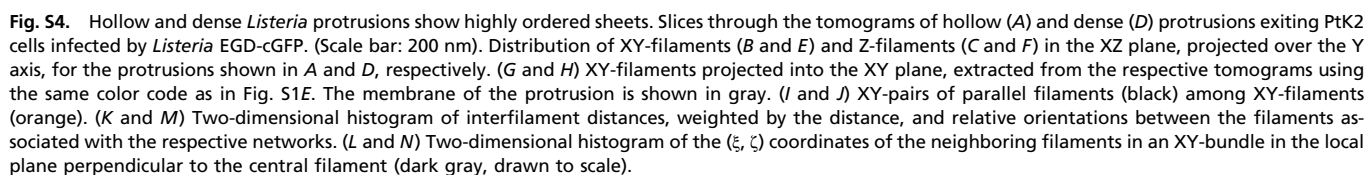


Fig. S3. *Listeria* protrusion shows hexagonal bundles. (A) Electron micrograph (stitched projection images) of a protrusion formed by *Listeria* EGD-cGFP at the surface of a PtK2 cell. (Scale bar: 200 nm.) The right box (Fig. 2A) indicates the location of the slice through the tomogram shown in Fig. 2A. (B) Slice through the tomogram at the position indicated by the left box (B) in A. (Scale bar: 200 nm.) (C) XY-filaments projected into the XY plane using the same color code as in Fig. S1E. The plasma membrane of the protrusion is shown in gray. (D) Two-dimensional histogram of the (ξ, ζ) coordinates of the neighboring filaments in an XY-bundle in the local plane perpendicular to the central filament (dark gray, drawn to scale). (E) XY-pairs of parallel filaments (black) among XY-filaments (orange).



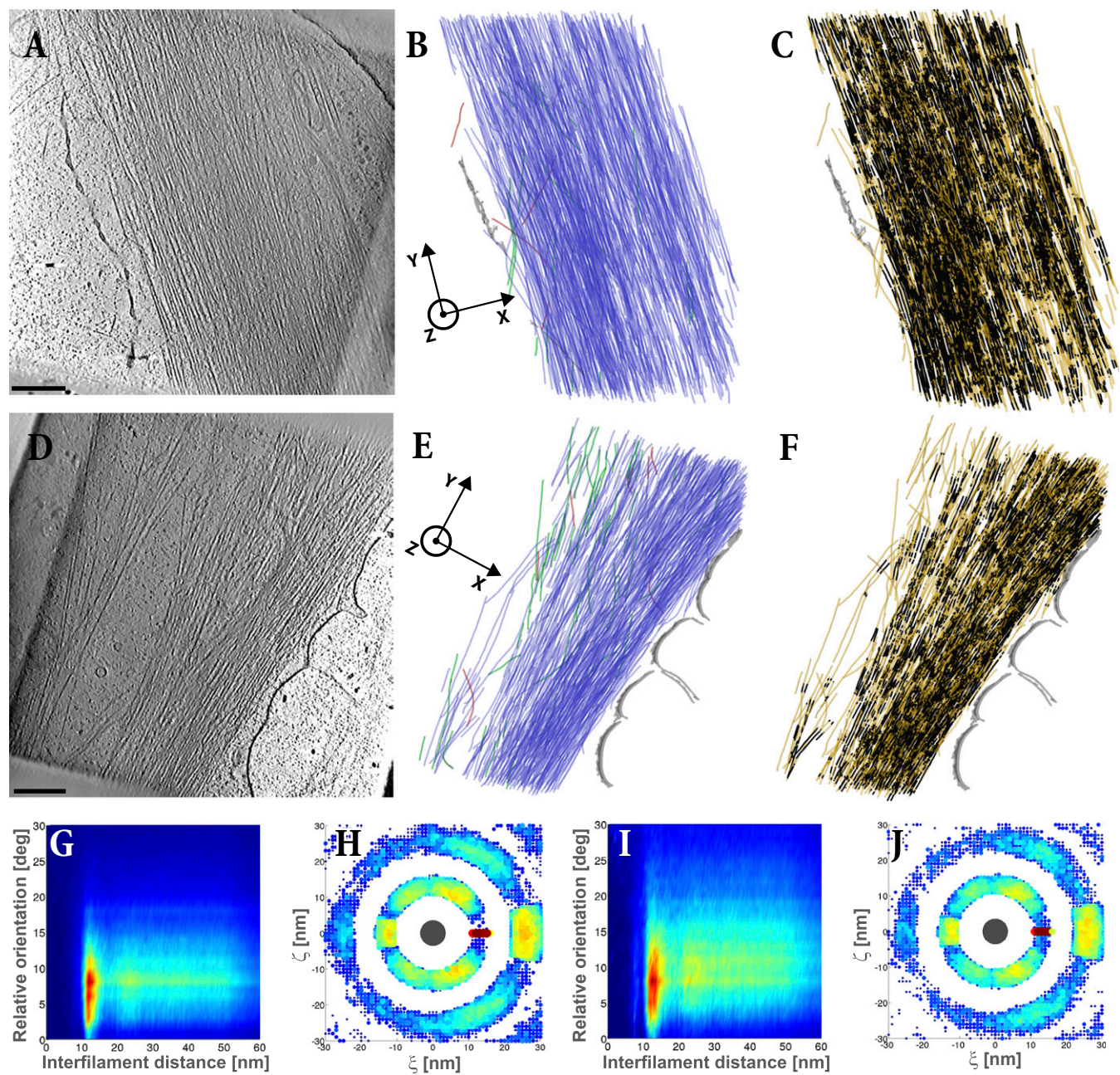


Fig. S5. Stress fibers are made of stacked sheets. (A and D) Slices through the tomograms of stress fibers in PtK2 cells. (Scale bar: 200 nm.) (B and E) XY-filaments projected into the XY plane, extracted from the tomograms shown in A and D, respectively, using the same color code as in Fig. S1E. The plasma membrane is shown in gray. (C and F) XY-pairs of parallel filaments (black) among XY-filaments (orange). (G and I) Two-dimensional histograms of interfilament distances, weighted by the distance, and relative orientations between the filaments associated with the respective networks. (H and J) Two-dimensional histograms of the (ξ, ζ) coordinates of the neighboring filaments in an XY-bundle in the local plane perpendicular to the central filament (dark gray, drawn to scale).

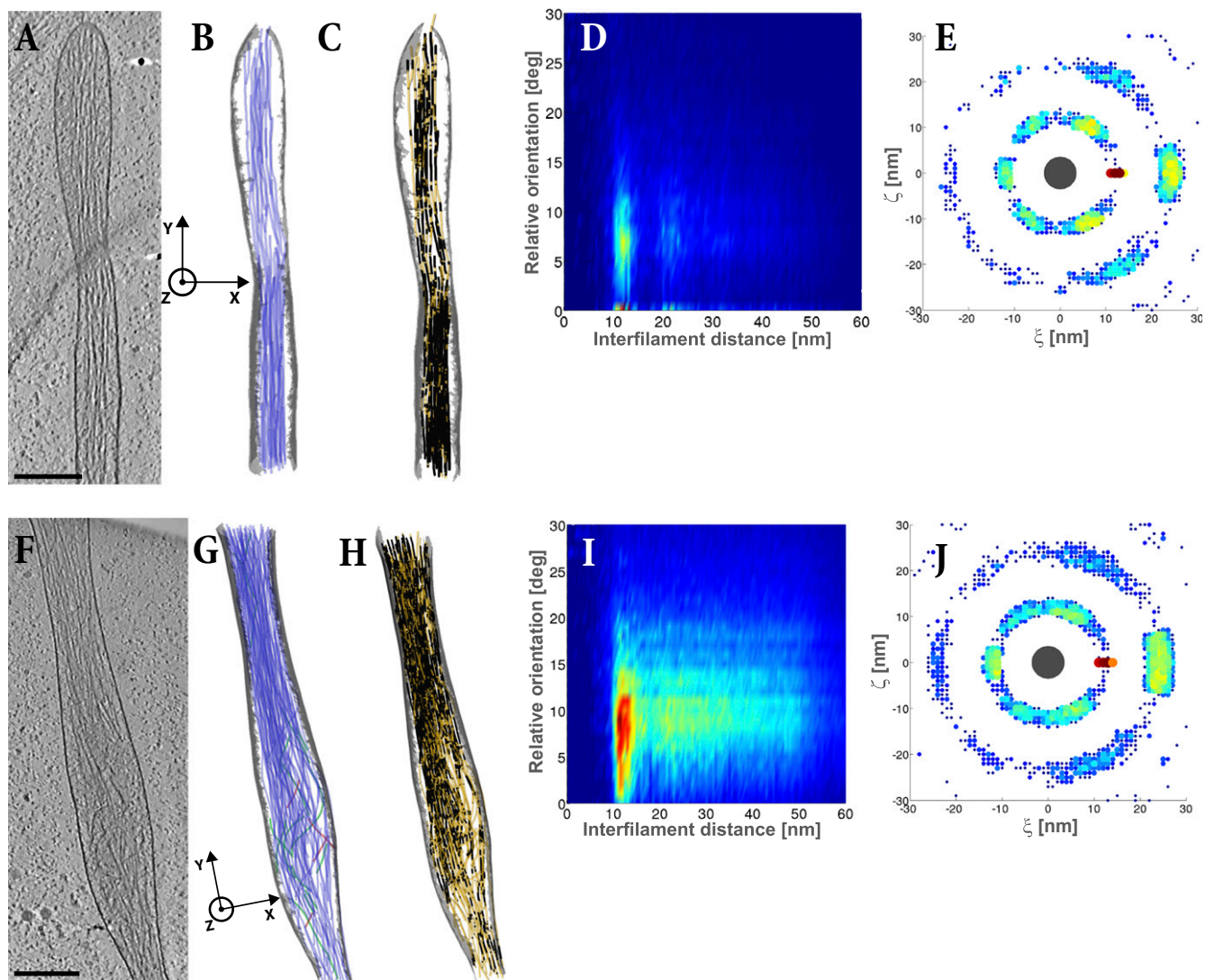


Fig. S6. Filopodia contain hexagonal bundles. (A and F) Slices through the tomograms of filopodia in PtK2 cells. (Scale bar: 200 nm.) (B and G) XY-filaments projected into the XY plane, extracted from the tomograms shown in A and F, respectively, using the same color code as in Fig. S1E. The plasma membrane is shown in gray. (C and H) XY-pairs of parallel filaments (black) among XY-filaments (orange). (D and I) Two-dimensional histograms of interfilament distances, weighted by the distance, and relative orientations between the filaments associated with the respective networks. (E and J) Two-dimensional histograms of the (ξ , ζ) coordinates of the neighboring filaments in an XY-bundle in the local plane perpendicular to the central filament (dark gray, drawn to scale).

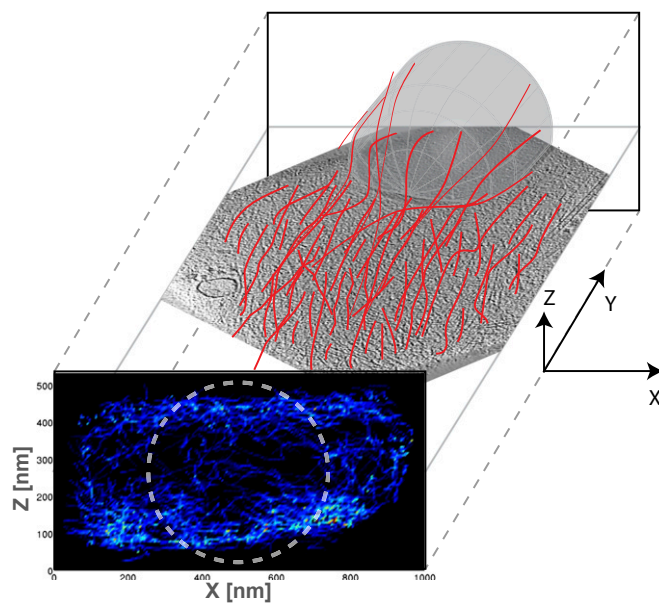


Fig. S7. Scheme illustrates the inhomogeneity of our actin-tail data about the long axis, Y, of the network. Actin filaments are represented in red. A slice through a tomogram of a cytoplasmic comet tail is shown in the XY plane. The cell wall of the bacterium is shown in transparent gray. The filament distribution projected over the Y axis is shown in the XZ plane.

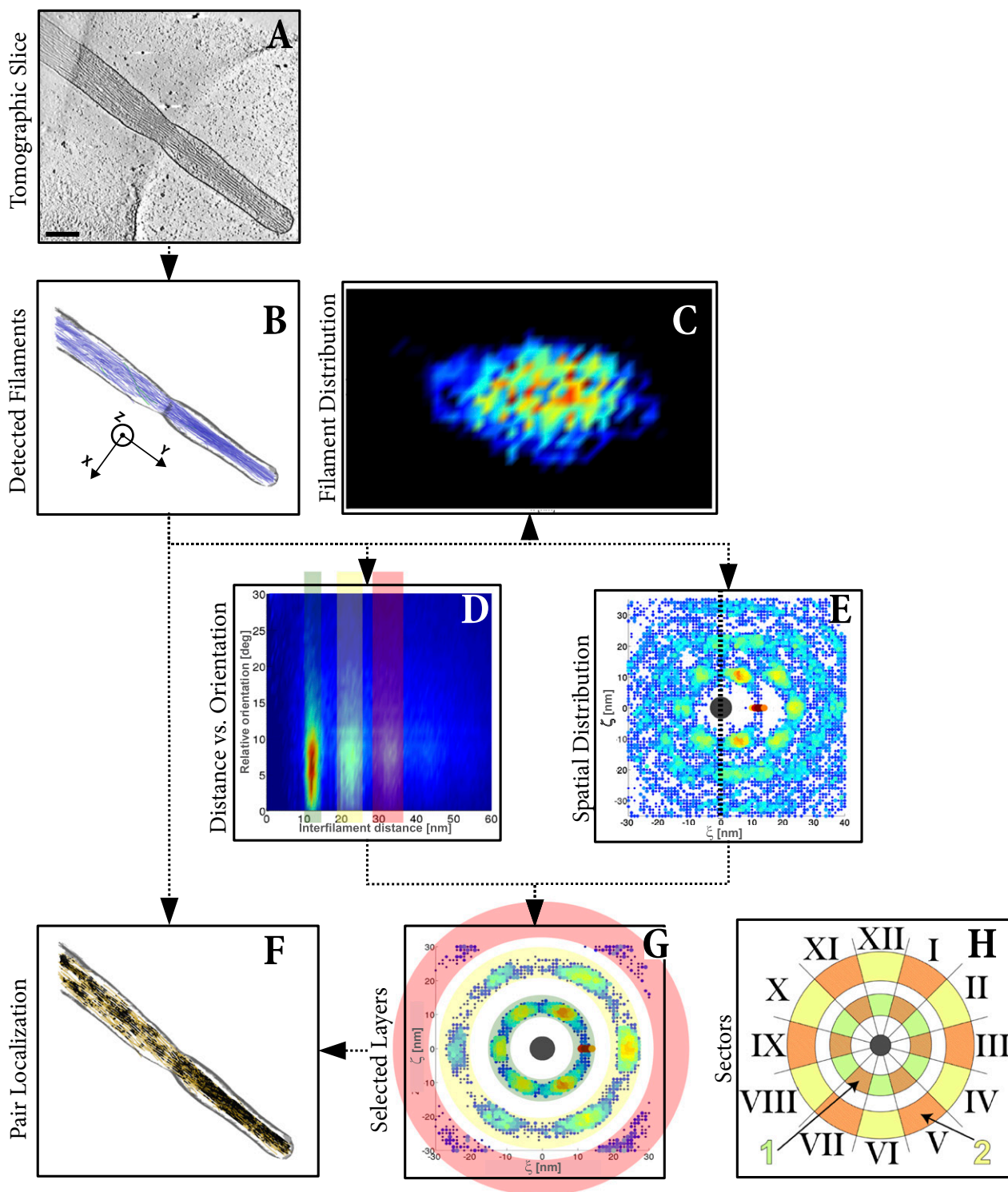


Fig. S8. Work flow to visualize the 3D architecture and the packing of actin filaments on a filopodium dataset obtained by CET. (A) Slice through the denoised tomogram of a filopodium. (Scale bar: 200 nm.) (B) XY-filaments projected into the XY plane. The color of the filaments corresponds to their angle with respect to the Y axis: 0–15° (blue), 15–30° (green), 30–45° (red). The plasma membrane is shown in gray. (C) XY-filament distribution in the XZ plane, projected over the Y axis. The color scale ranges from high occurrence (red) to low occurrence (blue). (D) Two-dimensional histogram of interfilament distances, weighted by the distance, and relative orientations between the filaments, with zones of interest highlighted in green, yellow, and red. deg, degrees. (E) Two-dimensional histogram of the (ξ , ζ) coordinates of the neighboring filaments in the local plane perpendicular to the central filament (dark gray, drawn to scale). (F) XY-pairs of parallel filaments (black) among XY-filaments (orange). (G) Two-dimensional histogram of the (ξ , ζ) coordinates of the neighboring filaments in an XY-bundle in the local plane perpendicular to the central filament (dark gray, drawn to scale). Layers 1, 2, and 3 shown in D are displayed using the same color code. (H) Sectors used as a visual aid to complement the 2D histogram of the filaments belonging to an XY-bundle, as shown in G. Layers 1 (green) and 2 (yellow) are also represented. The diameter of the central filament is drawn to scale and displayed in dark gray. The orange area corresponds to the main area of interest observed in our data.

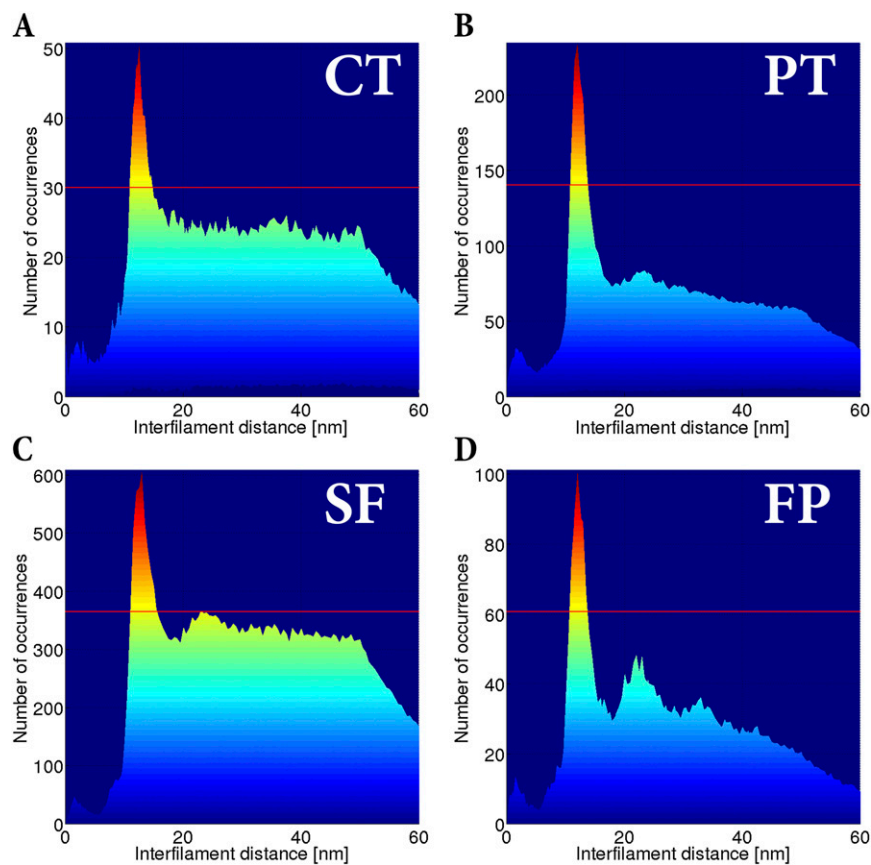


Fig. S9. Distance range criterion for the parallel filaments. Histograms of the interfilament distances, weighted by the distance, in the cytoplasmic comet tail (CT) (A), protrusion (PT) (B), stress fiber (SF) (C), and filopodia (FP) (D) overall networks are shown. The red line is drawn at a number of occurrences corresponding to 60% of the peak maximum, defining the most common interfilament spacing. The range includes all distances around the peak, with a number of occurrences above this limit (Table S1).

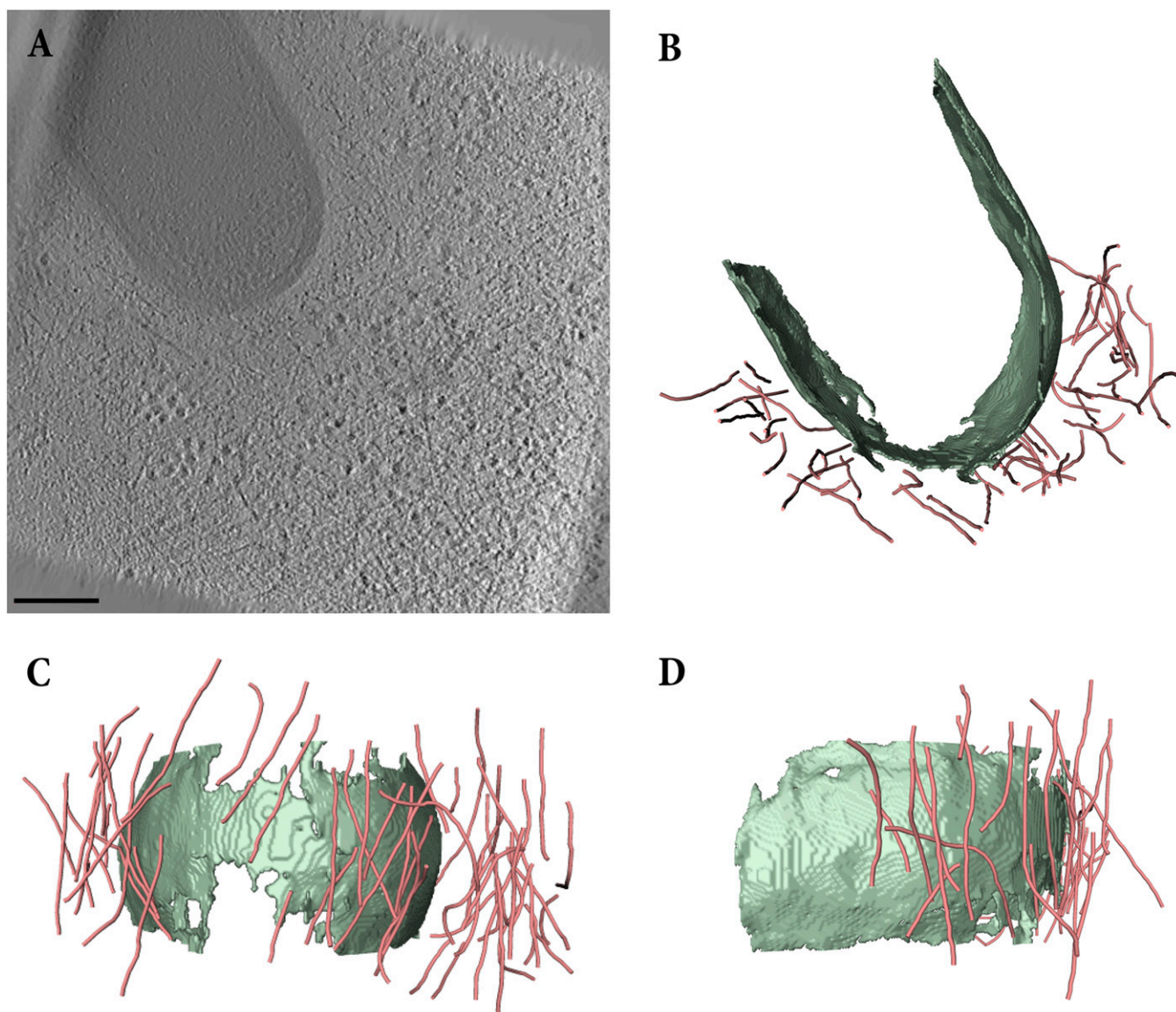


Fig. S10. Actin cloud in the cell interior shows short Z-filaments. (A) Slice through the tomogram of a cytoplasmic actin cloud assembled at the surface of *Listeria* EGD (BUG 600) in a PtK2 cell. (Scale bar: 200 nm.) (B–D) Top and side views of the Z-filaments (pink) in the actin cloud. The cell wall of the bacterium is shown in green.

Table S1. Parameters of the cellular actin networks

Parameter	Cytoplasmic tails	Protrusions	Stress fibers	Filopodia
<i>N</i> (tomograms)	5	9	8	4
XY-filaments, %	73 ± 15	89 ± 5	98 ± 1	99 ± 1
XY-filaments mean length, nm	170 ± 76	238 ± 133	243 ± 175	337 ± 261
Z-filaments mean length, nm	154 ± 56	153 ± 49	*	*
Parallel filaments range, nm	10.9–14.8	10.8–13.8	11.0–15.6	10.7–13.8
Interfilament spacing, nm	12.8 ± 1.1	12.3 ± 0.8	13.3 ± 1.3	12.2 ± 0.9
XY-pairs range, %	6.8–20.7	11.7–34.8	38.4–63.3	51.1–71.6
XY-pairs mean, %	10.7 ± 5.0	20.0 ± 7.7	48.6 ± 8.6	61.4 ± 8.4
XY-sheets range, %	0.2–2.1	0.7–6.9	5.6–15.8	11.6–24.5
XY-sheets mean, %	0.7 ± 0.7	2.6 ± 2.0	10.3 ± 3.5	17.2 ± 5.5
XY-hexagonal bundles range, %	0–0.8	0.1–6.4	3.3–14.3	9.2–29.8
XY-hexagonal bundles mean, %	0.2 ± 0.3	1.5 ± 2.2	7.4 ± 3.8	18.8 ± 9.2
<i>N</i> (neighboring XY-filaments)	11 ± 6	15 ± 7	30 ± 13	29 ± 8

N (neighboring XY-filaments) is the mean of the number of neighboring XY-filaments per filament. The values of the uncertainties are ±1 SD.

*Not statistically significant.